# Iterative RF Pulse Design for Multidimensional, Small-Tip-Angle Selective Excitation

Chun-yu Yip,[1*] Jeffrey A. Fessler,[1,2] and Douglas C. Noll[2]

**The excitation *k*-space perspective on small-tip-angle selective excitation has facilitated RF pulse designs in a range of MR applications. In this paper, *k*-space-based design of multidimensional RF pulses is formulated as a quadratic optimization problem, and solved efficiently by the iterative conjugate-gradient (CG) algorithm. Compared to conventional design approaches, such as the conjugate-phase (CP) method, the new design approach is beneficial in several regards. It generally produces more accurate excitation patterns. The improvement is particularly significant when *k*-space is undersampled, and it can potentially shorten pulse lengths. A prominent improvement in accuracy is also observed when large off-resonance gradients are present. A further boost in excitation accuracy can be accomplished in regions of interest (ROIs) if they are specified together with "don't-care" regions. The density compensation function (DCF) is no longer required. In addition, regularization techniques allow control over integrated and peak pulse power. Magn Reson Med 54:908–917, 2005. © 2005 Wiley-Liss, Inc.**

**Key words: iterative pulse design; small tip angle; selective excitation; excitation *k*-space; constrained minimization**

The design of RF pulses for multidimensional, small-tip-angle selective excitation is facilitated by the excitation *k*-space perspective developed by Pauly et al. (1) under the small-tip-angle approximation to the Bloch equation. *k*-Space-based selective excitation has been used in a range of MR applications, such as functional MRI (fMRI) artifact correction (2), brain imaging with reduced field of view (FOV) (3), blood velocity measurement (4), parallel excitation using multiple transmit coils (5,6), and excitation inhomogeneity correction (7). The *k*-space perspective is popular because it provides a fairly accurate linear Fourier relationship between the time-varying gradient and RF waveforms, and the resulting transverse excitation pattern. The Fourier relationship can also be established for rotation angles (possibly large), provided that certain symmetry conditions are satisfied (8).

A common approach to small-tip-angle RF pulse design is to predetermine the gradient waveforms and thus the *k*-space trajectory, and then obtain the complex-valued RF waveform by sampling the Fourier transform of the desired excitation pattern along the trajectory. Afterwards, the sample values are compensated for density variation in the trajectory. Some researchers have designed pulses by adopting the conjugate-phase (CP) approach from image reconstruction (9,10), which accounts for off-resonance effects and thus can correct for it to some extent (11,12).

These conventional approaches are nonideal in several regards. First, in terms of minimizing excitation error, they generally produce pulses that are suboptimal even with respect to the linear design model. This design suboptimality is an eradicable source of excitation error, on top of the intractable amount of error due to the small-tip-angle approximation underlying excitation *k*-space. The excitation error due to design suboptimality is particularly large when the trajectory undersamples *k*-space, or when large spatial variations of off-resonance are present (11). To compensate for the effects of off-resonance gradients to some extent, Noll et al. (13) suggested the use of a sophisticated density compensation function (DCF) in the CP method; however, that function is spatially variant and may not be readily extended to the excitation case. In fact, it is generally difficult and time-consuming to obtain an accurate DCF evaluation (see, for example, Ref. 14). Erroneous DCF evaluations contribute significantly to excitation error.

In addition to their suboptimality, the current design approaches cannot handle the secondary objective of minimizing integrated RF power due to specific absorption rate (SAR) considerations (15,16), or the hard constraint of peak RF power due to amplifier limitation (17). Also, they are unable to exploit the possibility of assigning spatial weighting to excitation error. These issues suggest that there is room for improvement in small-tip-angle RF pulse design methodology, which would benefit current applications and possibly foster future ones.

The inverse-problem nature of small-tip-angle RF pulse design suggests that an optimization approach can be beneficial. In fact, a range of optimization schemes have been used by researchers to design slice-selective 90°, inversion, and spin-echo pulses (e.g., Refs. 15–20). Those optimal pulses, designed with respect to the exact Bloch equation system, achieve very accurate slice profiles. It is a natural extension to apply some of those schemes to the small-tip-angle design problem. Another inspiration for a better design method is the recent development of iterative image reconstruction algorithms (21,22) that are also optimization schemes. Iterative reconstruction methods produce improved image quality relative to the CP and gridding methods (21–23). The analogy between image reconstruction and small-tip-angle RF pulse design (11) suggests that similar iterative optimization schemes can be applied to the latter.

In this context, we propose that small-tip-angle RF pulses can be designed via minimization of a quadratic

[1]Department of Electrical Engineering and Computer Science, University of Michigan, Ann Arbor, Michigan, USA.

[2]Department of Biomedical Engineering, University of Michigan, Ann Arbor, Michigan, USA.

Grant sponsor: NIH; Grant number: DA15410.

*Correspondence to: Chun-yu Yip, Functional MRI Laboratory, University of Michigan, 2360 Bonisteel Ave, Ann Arbor, MI 48109-2108. E-mail: chunyuy@umich.edu

Received 28 July 2004; revised 26 April 2005; accepted 26 April 2005.

DOI 10.1002/mrm.20631

Published online 9 September 2005 in Wiley InterScience (www.interscience.wiley.com).

cost function that consists of an excitation error term and regularization terms that control pulse power. The minimization problem can be solved iteratively via the conjugate-gradient (CG) method (22). Off-resonance during excitation, particularly in the case of long pulses, has a significant impact on the excitation accuracy (11,12), and thus its effects are included in our design model.

In the following section we formulate small-tip-angle RF pulse design as an optimization problem, and discuss its numerical solution. We then present the results of a Bloch equation simulation results, which show quantitatively the benefits of the iterative design method in terms of excitation accuracy when excitation *k*-space is undersampled or off-resonance is present. We also investigate the trade-off between excitation accuracy and pulse power. Finally, we present results from scanner experiments.

## THEORY

Let us define the complex function $M(\mathbf{x}; b)$ as the transverse magnetization pattern resulting from the Bloch equation, with input complex RF pulse envelope $b(t)$ and predetermined real gradient waveforms $\mathbf{g}(t) = [g_x(t)\ g_y(t)\ g_z(t)]^T$, $t \in [0, T]$. We assume that all magnetization is initially fully relaxed and aligned with the $+z$ axis, and has equilibrium magnitude $M_o$. For tip angles of 0–90°, the complex representation can unambiguously specify magnetization. In the small-tip-angle regime, one can design an optimal RF pulse by minimizing a cost function that includes an excitation error measure and a pulse energy term that allows for a soft constraint on the integrated RF pulse power:

$$b_{opt} = \underset{b}{\operatorname{argmin}} \left\{ \int_{-\infty}^{\infty} |M(\mathbf{x}; b) - D(\mathbf{x})|^2 W(\mathbf{x})\, d\mathbf{x} + \beta \int_0^T |b(t)|^2\, dt \right\}, \quad [1]$$

which is subject to the peak RF power hard constraint:

$$|b(t)|^2 \le C, \quad t \in [0, T]. \quad [2]$$

In Eq. [1], the complex function $D(\mathbf{x})$ is the desired magnetization pattern, the real function $W(\mathbf{x})$ is a user-defined error weighting pattern that can cover the FOV or any arbitrary ROIs, and $\beta$ is a regularization parameter that controls integrated power (IP) based on (SAR) considerations. $C$ is a certain constant that depends on the RF amplifier peak power (PP) limitation. A similar version of this problem for large-tip excitation was solved in Refs. 15–17 for the 1D and constant-gradient case, but it was a difficult and time-consuming optimization problem due to the Bloch equation nonlinearity. In the small-tip-angle regime, linearization of the Bloch equation can reduce Eq. [1] to a more easily solvable form.

Using the small-tip-angle approximation, Pauly et al. [1] derived that $M(\mathbf{x}; b)$ can be approximated by a Fourier integral, and off-resonance during excitation can be easily incorporated by an extra exponential factor (11,12):

$$M(\mathbf{x}; b) \approx i\gamma M_o \int_0^T b(t) e^{i\mathbf{k}(t)\cdot\mathbf{x} + i\Delta\omega(\mathbf{x})[t-T]}\, dt, \quad [3]$$

where $\gamma$ denotes the gyromagnetic ratio, $\Delta\omega(\mathbf{x})$ represents resonance frequency offsets, and $\mathbf{k}(t)$ is any realizable excitation *k*-space trajectory given by the integral of the remaining gradient area:

$$\mathbf{k}(t) = -\gamma \int_t^T \mathbf{g}(\tau)\, d\tau. \quad [4]$$

An RF pulse is generally defined discretely in a pulse sequence, processed by a digital-to-analog (D/A) converter, and then played out in the coil via RF circuitry. Let $b_j$, $j = 0, \ldots, N_t - 1$ be the pulse samples in the pulse sequence, and $\Delta t$ be the sampling period. If the temporal point spread function (PSF)[1] in the pulse that is physically played out is narrow, then we can approximate Eq. [3] as

$$M(\mathbf{x}; b) \approx i\gamma M_o \sum_{j=0}^{N_t-1} b_j e^{i\mathbf{k}(t_j)\cdot\mathbf{x} + i\Delta\omega(\mathbf{x})[t_j - T]} \Delta t. \quad [5]$$

We sample $M$ at Cartesian spatial locations $\{\mathbf{x}_i\}_{i=0}^{N_s-1}$, and express Eq. [5] in matrix-vector multiplication form:

$$\mathbf{m} \approx \mathbf{A}\mathbf{b} \quad [6]$$

where $\mathbf{m} = [M(\mathbf{x}_0; b) \cdots M(\mathbf{x}_{N_s-1}; b)]^T$, $\mathbf{b} = [b_0 \cdots b_{N_t-1}]^T$, and the elements of the $N_s \times N_t$ system matrix are

$$a_{i,j} = i\gamma M_o e^{i\mathbf{k}(t_j)\cdot\mathbf{x}_i + i\Delta\omega(\mathbf{x}_i)[t_j - T]} \Delta t. \quad [7]$$

Now we can obtain the RF pulse samples by solving

$$\hat{\mathbf{b}} = \underset{\mathbf{b}}{\operatorname{argmin}} \{\|\mathbf{A}\mathbf{b} - \mathbf{d}\|_{\mathbf{W}}^2 + \beta \mathbf{b}'\mathbf{b}\}, \quad [8]$$

subject to

$$|b_j|^2 \le C, \quad j = 0, \ldots, N_t - 1, \quad [9]$$

in which $\mathbf{d}$ is a vector that contains samples of the desired pattern at the corresponding spatial locations, $'$ denotes the complex conjugate transpose, and $\mathbf{W}$ is an $N_s \times N_s$ diagonal matrix containing the user-selected error weighting $\{W(\mathbf{x}_i)\}_{i=0}^{N_s-1}$. The $\mathbf{W}$-weighted 2-norm denotes $(\mathbf{A}\mathbf{b} - \mathbf{d})'\mathbf{W}(\mathbf{A}\mathbf{b} - \mathbf{d})$. $\mathbf{W}$ can be used to specify spin-free regions as "don't care" regions.

[1]The RF pulse being physically played out can be modeled as a pulse sample weighted "train of Dirac impulses" convolved with a time-invariant PSF. The temporal spreading can arise from D/A converter characteristics and RF circuit impulse response functions. In the present analysis we ignored this spreading effect, although it could have been incorporated easily.

The dimensions of matrix **A** depend on the sample spacing in **m** and **d**, and the length of the RF pulse being designed. Indeed, sample spacing in **m** and **d** dictates whether the system of equations $\mathbf{Ab} = \mathbf{d}$ is overdetermined or underdetermined when no regularization is applied. We found that it is generally beneficial, in terms of excitation error evaluated over the continuous spatial domain, to sample $D(\mathbf{x})$ finely (with higher resolution than that supported by the trajectory) so that the unregularized design problem $\mathbf{Ab} = \mathbf{d}$ is overdetermined.

We can invoke the Karush-Kuhn-Tucker (KKT) theorem in nonlinear optimization theory (24) to solve Eqs. [8] and [9], as detailed in the Appendix. The optimal solution suggests that a magnitude-constrained RF pulse can be designed via

$$\hat{\mathbf{b}} = \arg\min_{\mathbf{b}} \{\|\mathbf{Ab} - \mathbf{d}\|_{\mathbf{W}}^2 + \beta \mathbf{b}'\mathbf{b} + \mathbf{b}'\mathbf{\Lambda}\mathbf{b}\}, \qquad [10]$$

where $\mathbf{\Lambda} = diag(\lambda_j)$, and $\lambda_j$, $j = 0, \ldots, N_t - 1$ denote regularization parameters that control the magnitude of individual RF pulse samples. One can describe $\mathbf{b}'\mathbf{\Lambda}\mathbf{b}$ as the "local" regularization term for controlling PP, whereas $\beta\mathbf{b}'\mathbf{b}$ is the "global Tikhonov regularization term, often used in other imaging applications, for controlling integrated RF power. Regularization may degrade the fit between the resulting and desired patterns in exchange for reducing pulse power. The trade-off can be tuned by the regularization parameters. Slight Tikhonov regularization is generally needed to ensure that pulses are physically realizable.

For a certain set of regularization parameters, the designed pulse can be constraint-violating, and thus the parameters must be incremented. One heuristic approach used to search for a good set of parameter values is to iteratively check IP and PP, increment $\beta$ in the case of an IP violation, and $\lambda_j$ in the case of a PP violation at pulse sample $b_j$, and then redesign until the IP is acceptable and the PP is within amplifier limitation. This "check-and-redesign" process is sensible because for practical pulse design problems the RF power constraints are often not violated. The PP constraint violation may occur at very few time points, if at all. Thus all or most of the regularization parameters can be zero. In such cases, the heuristic approach is computationally economical because it avoids the need to simultaneously solve for the optimizing pulse and KKT multipliers (see Appendix).

For Eq. [10], if the regularization parameter values are fixed, then $\hat{\mathbf{b}} = (\mathbf{A}'\mathbf{W}\mathbf{A} + \mathbf{R})^{-1}\mathbf{A}'\mathbf{W}\mathbf{d}$ , where $\mathbf{R} = \mathbf{I}\beta + \mathbf{\Lambda}$. This analytical solution involves a matrix inversion, which is a computationally intensive $O(N_t^3)$ operation. To reduce the complexity, we instead apply the $O(N_t^2)$ iterative CG algorithm (22), which converges to the optimizing pulse over iterations. The complexity reduction can be highly significant for the design of long pulses. One can initialize CG with a CP design for a good initial guess. Alternatively, one can initialize with a zero pulse without loss of excitation accuracy, provided that enough iterations are used.

## MATERIALS AND METHODS

### Pulse Computations

RF pulses were computed offline with Matlab 6.5 (MathWorks Inc., Natick, MA, USA). They were spatially selective in the two transverse dimensions. In all cases we used single-shot spiral-out excitation *k*-space trajectories (25) with the following gradient parameters: maximum magnitude = 4 G/cm, maximum slew rate = 18000 G/cm/s, and sampling period = 4 $\mu$s. Unless otherwise stated for specific experiments, we used a trajectory that supported 0.5 cm $\times$ 0.5 cm resolution, and an excitation field of view (XFOV) of 18 cm diameter, resulting in a pulse duration of 9.01 ms.

The desired patterns had a common resolution of 0.25 cm $\times$ 0.25 cm. In the simulations, the desired pattern was a 15 cm $\times$ 5 cm block, with magnitude 0.5 (unit magnitude corresponded to 90° tip angle), perfectly sharp edges, and zero phase everywhere. Excitation error was equally weighted within either a circular ROI (20 cm diameter) or an elliptic reduced ROI (with the length of the major and minor axes being 18 cm and 12 cm, respectively). Outside the ROIs were "don't-care" regions assigned with zero error weighting. This setup simulated inner volume excitation of a block inside a human skull for spectroscopic imaging (26), for which the elliptic ROI covered the head within the FOV. The desired patterns and ROIs in the scanner experiments are detailed in the Scanner Experiments section.

The CG algorithm in the iterative method was initialized with a zero pulse and run for 15 iterations for sufficient convergence. Except in simulation III, we used Tikhonov regularization with $\beta = 2.25$ to avoid physically unrealizable pulse designs. Off-resonance effects were considered in simulation II and scanner experiment II.

For comparison with the iterative method, we used the CP algorithm as the standard. DCFs were calculated based on the Jacobian formula (27). When resonance frequency offsets are not incorporated, CP is equivalent to the method of sampling the Fourier transform of the desired pattern along the trajectory, provided that no interpolation error is introduced in the sampling step. Such interpolation errors can be made arbitrarily small by zero-padding the target pattern before transformation.

### Numerical Simulations

To evaluate the RF pulses, we performed numerical simulations of the Bloch equation with Matlab. The Bloch simulation was over a 2D grid covering a 20 cm $\times$ 20 cm region, with 0.25 cm $\times$ 0.25 cm resolution. Relaxation effects were ignored. In simulation II, a field map was incorporated in the Bloch simulator. For each excitation result from the Bloch simulator ($\mathbf{m}_{bl}$), we calculated the normalized root-mean-square excitation error (NRMSE) with respect to the desired pattern. The NRMSE was defined as $\|\mathbf{m}_{bl} - \mathbf{d}\|_{\mathbf{W}}/\|\mathbf{d}\|_{\mathbf{W}}$. Note that in each simulation study the same **W** was used for both the CP and iterative methods, and it covered the same ROI incorporated in the iterative scheme.

### Simulation I: *k*-Space Undersampling

The goal of simulation I was to compare the CP and iterative methods used in conjunction with trajectories that

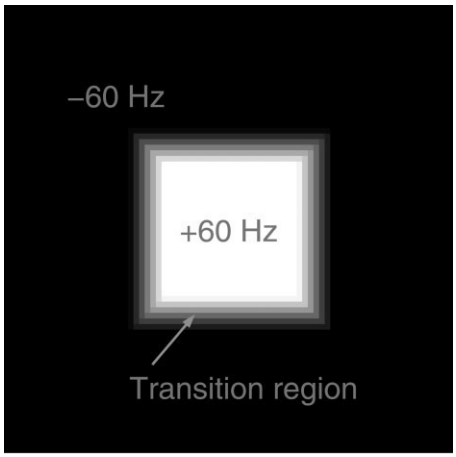


FIG. 1. Field map incorporated in the Bloch simulator and design methods in simulation II.

undersample excitation *k*-space. The spiral-out trajectories that were tested covered a fixed range in *k*-space, while the sampling interval was varied, leading to XFOV diameters ranging from 10 cm to 22 cm. For each XFOV diameter value, we computed the corresponding RF pulse designed via the CP and iterative methods. The iterative methods used either the circular or elliptic ROI. Gradient and RF pulse waveforms were then fed into the Bloch simulator, and the within-ROI NRMSE was computed.

### Simulation II: Off-Resonance Correction

We compared the abilities of the design methods in correcting for off-resonance effects during excitation. In the Bloch simulator, we incorporated a field map with flat regions in the center (+60 Hz) and background (−60 Hz), bridged by a linear transition region (Fig. 1). The width of the linear transition region was varied to represent different roughness values of the field map, with the central +60 Hz region fixed. For each transition steepness value, we simulated pulses designed with the field-map-incorporated CP and iterative method, using either the circular or elliptic ROI. In all cases the NRMSE was evaluated *only* within the transition region inside the ROIs.

### Simulation III: RF Pulse Power Management

Simulation III demonstrated the use of regularization for controlling IP and PP. The iteratively designed pulse in simulation I, with circular ROI, XFOV = 13 cm, and $\beta$ = 2.25, was treated as the original pulse. In two separate studies we investigated reducing its IP by 50% and its PP by 75%.

To reduce the IP we redesigned the original pulse by iteratively incrementing $\beta$ by 1.0 and rerunning the iterative scheme until the IP was below 50% of the original. To reduce the PP we redesigned the original pulse by iteratively locating pulse samples that violated the peak magnitude constraint (50% of the original peak), incrementing the local regularization parameters $\{\lambda_j\}$ at those violation points by 1.0, and rerunning the iterative scheme until the peak RF power was below 50% of the original. While the local regularization parameters were varied, we kept the original Tikhonov regularization ($\beta$ = 2.25).

We compared the NRMSE penalty induced by regularization with that induced by simply scaling the original pulse by $1/\sqrt{2}$ or clipping at half of its maximum magnitude.

### Scanner Experiments

Scanner experiments were performed on a GE 3 T Signa Scanner (GE Healthcare, Milwaukee, WI, USA) using a spherical homogeneous water phantom (GE Healthcare). 2D excitation patterns were imaged by a spin-echo (SE) spiral-out pulse sequence in which the slice-selective sinc pulse was replaced by the 2D pulse designs. The 180° pulse was slice-selective for refocusing the slice being imaged. Prescans for ROI and field map (experiment II) were acquired by a gradient-echo (GRE) spiral-out sequence. Eight acquisition interleaves were used in all sequences to minimize the off-resonance effect during acquisition. Common imaging parameters were as follows: slice thickness = 3.0 mm, FOV = 20 cm, matrix size = 64 × 64, TR = 1 s, and TE = 40 ms (SE) or 7.6 ms (GRE). In each of the two experiments, flip angles of the patterns being compared were matched via proper scaling of the pulses. For the 2D pulses, gradient waveforms for excitation were shifted forward by 145 μs to compensate for the delay between RF and gradient channels. Images were reconstructed from the scanner data using a fast implementation of the off-resonance compensated CP method (9). The implementation used field maps estimated from two images acquired with a TE difference of 2 ms (28). The use of an SE sequence with multiple interleaves and an off-resonance compensated reconstruction scheme ensured that image artifacts due to off-resonance during acquisition were insignificant.

### Experiment I: Variable-Density Trajectory

Variable-density spiral trajectories (29,30), which undersample *k*-space regionally, can be useful for reducing pulse length. We investigated whether aliasing could be alleviated when those trajectories were used in conjunction with the iterative design method. Excitation patterns produced by an identical variable-density trajectory but different RF pulse designs were imaged and compared.

The variable-density spiral-out trajectory we deployed adequately sampled excitation *k*-space near the origin (XFOV = 18 cm), and undersampled by a factor of 2.5 in the high-frequency region (Fig. 2). The pulse length was 4.65 ms, and the durations of the adequate-sampling and transition (from adequate-sampling to undersampling) segments were 1.0 ms and 0.8 ms, respectively. To simulate ROI determination in human scanning, we prescanned the phantom with a GRE spiral sequence with a slice-selective sinc pulse, and thresholded the resulting image at 0.3 of its maximum magnitude. CP and (ROI-incorporated) iterative methods were then applied to compute two RF pulses for the desired pattern, which was a uniform disc (6 cm in diameter) with sharp edges. Selective excitation of discs is useful in applications such as inner volume excitation (26) and 2D navigator pulses (31).

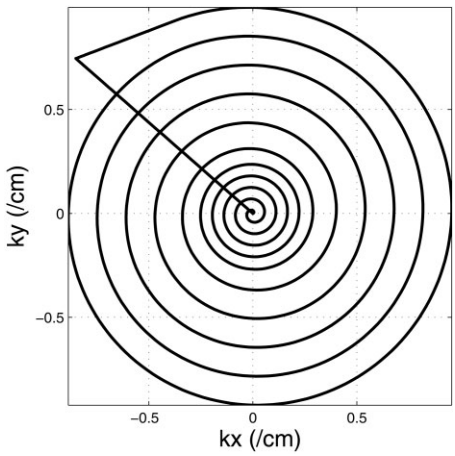


FIG. 2. Variable-density spiral trajectory deployed in scanner experiment I.

### Experiment II: Off-Resonance Correction

We experimentally compared off-resonance correction by the design methods. Three ferromagnetic metal pieces were attached to the phantom surface to create main field inhomogeneity. With the same 9.01-ms trajectory used in the simulations, we designed one pulse using the iterative method without field map incorporation, and two other pulses using CP and iterative methods with field map incorporation. As in the previous experiment, we prescanned the phantom and performed image thresholding to determine the ROI. The resulting excitation patterns were then imaged and compared.

The field map was estimated from two GRE images (28), with TE values of 7.60 ms and 8.60 ms. We masked it with the ROI and then smoothed it using a regularized weighted least-squares method (32) before incorporation. The desired pattern was an arbitrary "stripes" pattern that covered the entire phantom and demonstrated off-resonance correction well.

## RESULTS

### Simulation I: *k*–Space Undersampling

Figure 3 shows the within-ROI NRMSE vs. XFOV diameter for each design method in simulation I. Compared to CP, the iterative method, regardless of ROI specification, led to lower within-ROI NRMSE for all XFOV diameter values considered. When the XFOV diameter was 18 cm (an adequate XFOV for our desired pattern) the iterative method with the circular ROI outperformed CP, whereas the iterative method using the elliptic ROI outperformed CP by a slightly larger margin. The margins became significant larger when *k*-space was undersampled, revealing the excitation accuracy advantage of the iterative method and the further benefit of reducing the size of the ROI. With CP, *k*-space undersampling led to excitation aliasing within the ROI. The iterative method was efficacious in suppressing the aliasing effect because the effect was accounted for in the optimization cost function and was thus minimized. ROI size reduction gave extra degrees of freedom toward better excitation accuracy.

These results also suggest that a given desired excitation accuracy can be achieved with a shorter trajectory by using the iterative method instead of CP. The iteratively designed pulse at point iv in Fig. 3 produced within-ROI accuracy close to that obtained by CP at point i, but its pulse length was significantly shorter (6.62 ms at iv, and 9.01 ms at i).

Figure 4 shows the excitation patterns corresponding to points i–iv in Fig. 3, and Fig. 5 displays the gradient and RF (magnitude) waveforms corresponding to points ii–iv. Although the same *k*-space trajectory was deployed, the design methods produced significantly different RF pulses. The iteratively-designed pulse at point iii had a spike corresponding to a *k*-space location close to the origin, which could lead to a PP violation. Simulation III illustrates modification of the regularization for suppressing the spike.

### Simulation II: Off-Resonance Correction

Figure 6 shows the within-ROI NRMSE in the transition region plotted against the off-resonance gradient magnitude. Pulses designed with CP produced increasingly distorted excitation in the transition region as the region became steeper. The degradation was consistent with results from other research studies that reported that the analogous CP reconstruction method did not correct well for rough field maps (22). On the other hand, the iteratively designed pulses were relatively immune to large off-resonance gradients. The excitation performance degraded relatively slowly as the gradient increased. Specification of the elliptic ROI in the iterative method did not have much effect on excitation accuracy.

Figure 7a shows the excitation pattern obtained by a pulse designed with CP without field map incorporation,

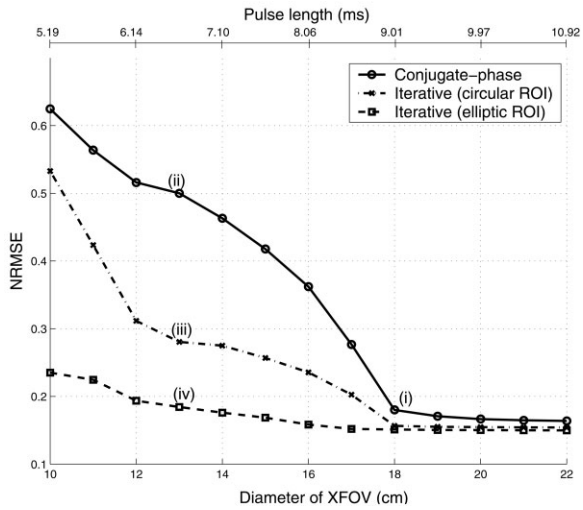


FIG. 3. Within-ROI excitation error resulting from RF pulses designed for spiral trajectories with different XFOVs (resolution held fixed). For a given trajectory, higher excitation accuracy was achieved by the iterative method, especially when the trajectory undersampled *k*-space. Reduction in the size of the ROI in the iterative method led to better within-ROI accuracy and higher tolerance of *k*-space undersampling. The excitation patterns and pulses at points i–iv are shown in Figs. 4 and 5.

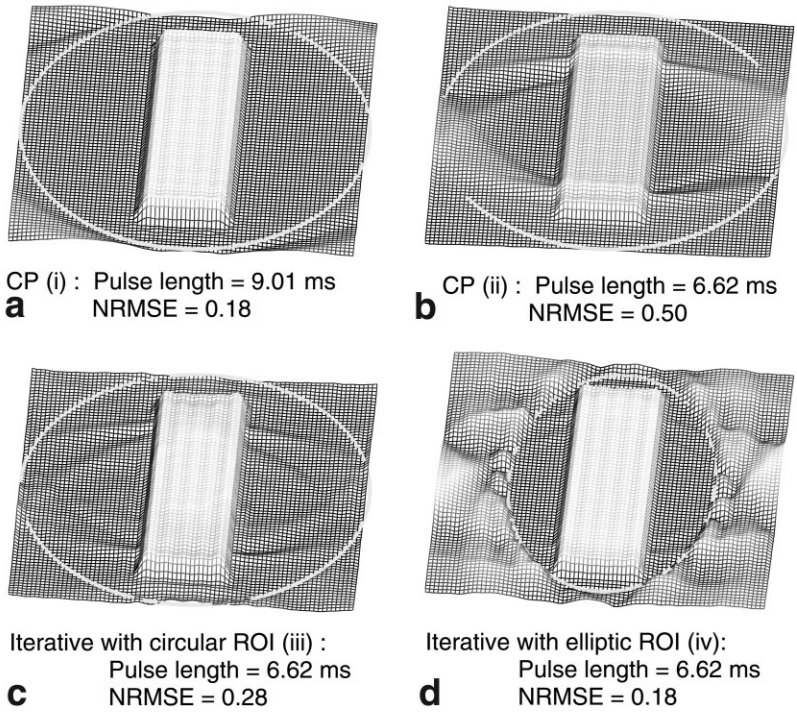


FIG. 4. Simulated excitation patterns corresponding to points i–iv in Fig. 3. Interior regions of the solid lines represent the circular or elliptic ROI. **a:** Pattern obtained by an adequate-sampling trajectory and a CP-designed pulse (i). **b-d:** Patterns obtained by a common trajectory that undersampled *k*-space (XFOV = 13 cm), accompanied by pulses designed with CP (ii) or the iterative method, with different ROI specifications (iii and iv).

at gradient magnitude 75 Hz/cm. Without field map incorporation the pattern was blurred due to off-resonance. The patterns that underlie points i–iii in Fig. 6 are juxtaposed in Fig. 7b–d. In regions with a zero off-resonance gradient, both design methods led to apparently equal excitation accuracy. However, the off-resonance gradient in the transition region differentiated the pulses. It is surprising that degradation in Fig. 7b turned out to be spatially localized.

### Simulation III: RF Power Management

Figure 8a shows the original pulse (blue; the same pulse as in the third panel of Fig. 5), and its redesigned versions (green and red) with Tikhonov regularization parameter β incremented to 5.25 and 11.25, respectively. Tikhonov regularization influenced the entire pulse, but predominantly on its early portion corresponding to the proximity of the *k*-space origin. Thus, we zoom in the pulses over the first half millisecond. The potentially unrealizable spike in the original pulse was significantly reduced with β = 5.25. It shrank by 50% with β = 11.25, while the IP was roughly halved relative to the original pulse. The pulses were significantly different from scaled versions of the original pulse.

Simulated profiles of these three pulses (at y = 0 cm) illustrated that IP was reduced at a low cost in excitation

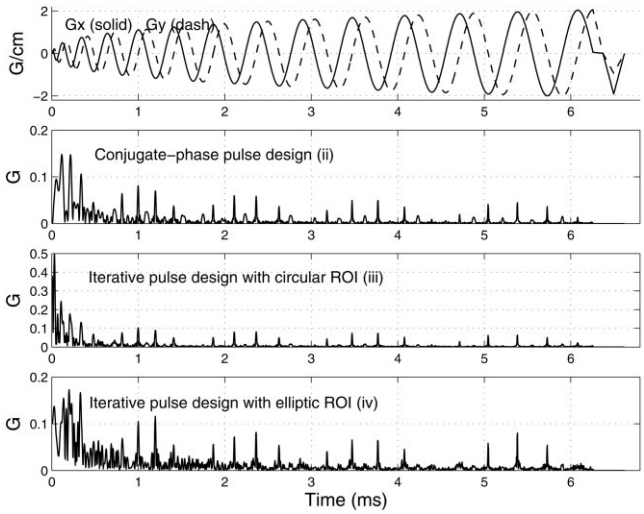


FIG. 5. Gradient and RF (magnitude) waveforms used to produce excitation patterns in Fig. 4b–d, corresponding to points ii–iv in Fig. 3. Although the same gradient waveforms and desired patterns were used, the RF pulse designs differed significantly (G = Gauss).

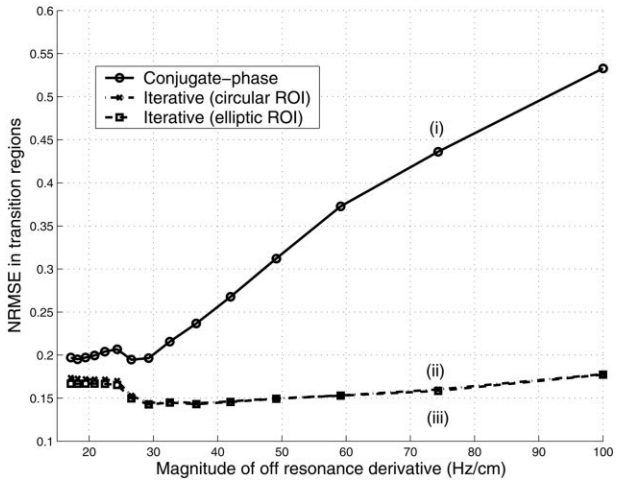


FIG. 6. NRMSE in the transition region within the ROI vs. the region's steepness. As the transition became more rapid, the performance of the CP-designed pulses degraded, whereas the iteratively designed pulses were relatively immune. Figure 7 shows excitation patterns at points i–iii.

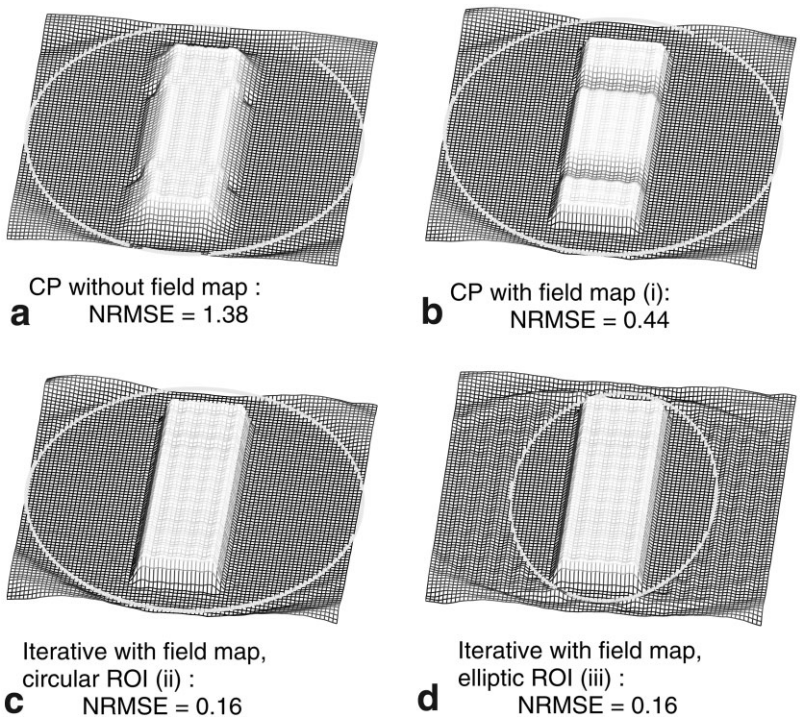


FIG. 7. **a:** Simulated excitation pattern obtained by a pulse designed using CP without incorporation of field map with transition region at 75 Hz/cm. **b-d:** Patterns obtained by pulses designed with the field-map-incorporated CP (point i in Fig. 6), and field-map-incorporated iterative method, with different ROI specifications (ii and iii). Interior regions of the solid lines represent the circular or elliptic ROI.

accuracy (Fig. 9). Scaling the original pulse by $1/\sqrt{2}$ was effective in cutting the original power by half, but the accuracy cost was significantly higher than that obtained with the Tikhonov regularization ($\beta = 11.25$).

Figure 8b illustrates the use of local regularization for PP reduction (spike suppression). The original pulse (blue) is juxtaposed with its redesigned version (red), as computed iteratively with local regularization parameters plotted in Fig. 8c. The redesigned pulse had PP 75% lower than the original compared to the original pulse clipped at half maximum, it was subtly different, and a profile simulation (at $y = 0$ cm) revealed that it led to significantly better excitation accuracy (Fig. 10). Note also that 50% spike suppression was achieved at a lower cost via local regularization compared to the globally influential Tikhonov regularization.

These two examples highlight how the optimization design approach modifies each pulse sample to seek an op-

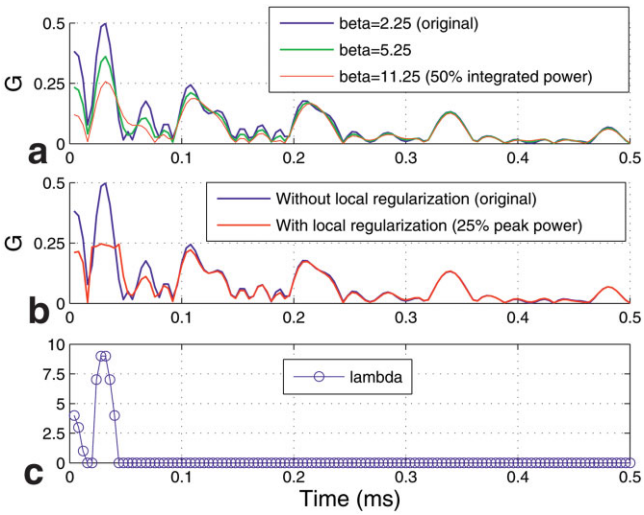


FIG. 8. **a:** The original pulse (blue; same pulse as in the third panel of Fig. 5) designed with Tikhonov regularization ($\beta = 2.25$). The pulse over the first half millisecond is plotted. Incrementing $\beta$ reduced the spike height and integrated pulse power (green and red). **b:** Original pulse (blue) and the pulse redesigned with local regularization. Its PP was about 25% of the original. **c:** Local regularization parameters used for the redesigned pulse in b. (Note: pulse magnitude is plotted in Gauss (G).)

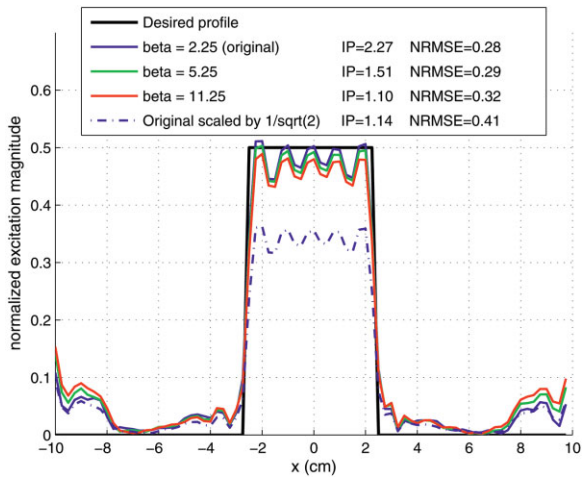


FIG. 9. Simulated pattern profiles at $y = 0$ cm, created by the original pulse (blue in Fig. 8a), the pulses redesigned with increased Tikhonov regularization (green and red in Fig. 8a), and the original pulse scaled by $1/\sqrt{2}$. With the regularized iterative design method, IP reduction was achieved with a low penalty in excitation accuracy. (Note: IP is in arbitrary units.)

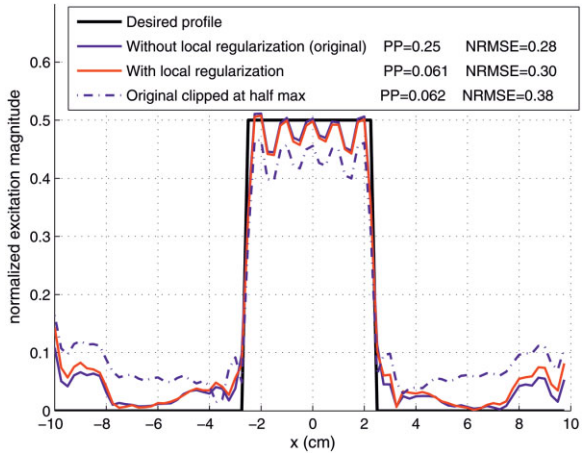


FIG. 10. Simulated pattern profiles at y = 0 cm, created by the original pulse (blue in Fig. 8b), the pulse (red in Fig. 8b) redesigned with local regularization parameters in Fig. 8c, and the original pulse clipped at half maximum. With the regularized iterative design method, a PP reduction was achieved with a low penalty in excitation accuracy. (Note: PP is in arbitrary units.)

timal trade-off between pulse power and excitation accuracy.

### Experiment I: Variable–Density Trajectory

An ROI was derived by thresholding a prescanned image of the phantom (Fig. 11a and b). Figure 11c–e are respectively the desired disc pattern and patterns excited by two pulses designed with the CP and iterative methods. Notice the aliasing effect in the CP pattern caused by undersampling of the high-spatial-frequency region, which contained significant energy because of the sharp disc edges. With the iteratively designed pulse the aliasing effect was significantly reduced, although the same trajectory was deployed. This was consistent with the results of simulation I, and likewise could be explained by inclusion of the aliasing phenomenon in the optimization cost function being minimized. Bloch simulation of the iteratively-designed pulse (Fig. 11f) revealed that the extra degrees of freedom in the outside-phantom region led to enhanced within-ROI accuracy.

### Experiment II: Off-Resonance Correction

Figure 12a and b show the "stripes" desired pattern and the pattern excited by an iteratively-designed pulse *before* the three metal pieces were attached to the phantom surface. Figure 12c shows the field map of the axial plane being imaged, which was inferior to the attached pieces. It revealed global distortion of the main field. Such field inhomogeneity is comparable to, for example, that found in brain regions near air cavities in the human skull. The same iteratively-designed pulse, now applied in a distorted field, excited a distorted pattern (Fig. 12d). The field map was then incorporated in the design methods. Figure 12e and f show patterns excited by pulses designed with the field-map-incorporated CP and iterative methods, respectively. The pattern distortion was significantly alleviated in both cases, but the iteratively designed pulse performed slightly better, as can be observed in regions with a high off-resonance gradient magnitude (white arrows). The accuracy in regions with low gradient magnitude was comparable. These observations were consistent with the results from simulation II. We expect the benefit of the iterative method to be more prominent when longer pulses are used (e.g., the 3D tailored RF pulse in Ref. 2).

## DISCUSSION

We have formulated an optimization approach to the pulse design problem for small-tip-angle selective excitation. We have shown that it is beneficial in several ways. In our simulations and experiments, iteratively designed pulses optimal with respect to the linear design system model, produced significantly more accurate excitation patterns from the Bloch equation system compared to the conventionally designed pulses. We found experimentally that this was generally true, even though the iteratively designed pulses were not optimized with respect to the nonlinear Bloch equation. The accuracy benefit was particularly prominent when the trajectory undersampled

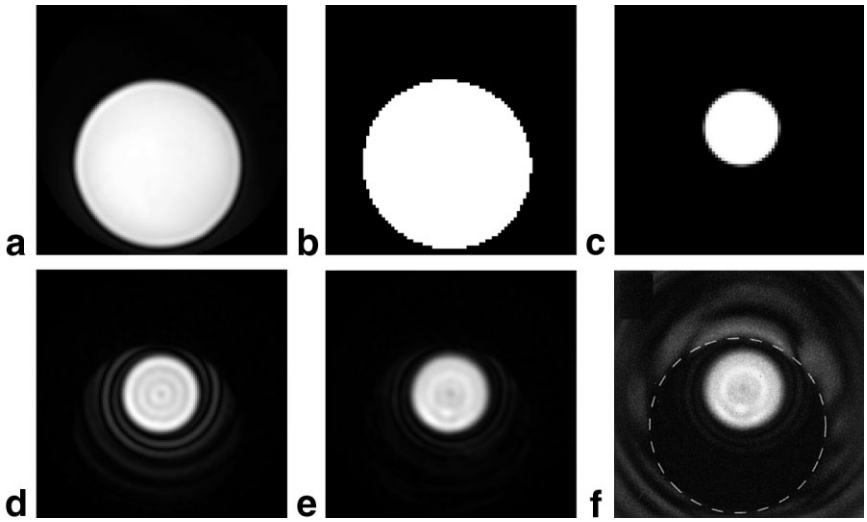


FIG. 11. (**a**) Prescanned image and (**b**) the ROI obtained by thresholding. **c:** Desired pattern. **d:** Measured pattern excited by the CP-designed pulse, which is plagued by aliasing excitation. **e:** Measured pattern excited by the pulse designed with the ROI-incorporated iterative method. Compared to the CP case, aliasing was significantly alleviated. **f:** Bloch simulation of the iteratively-designed pulse used in **e** (dashed line: ROI).

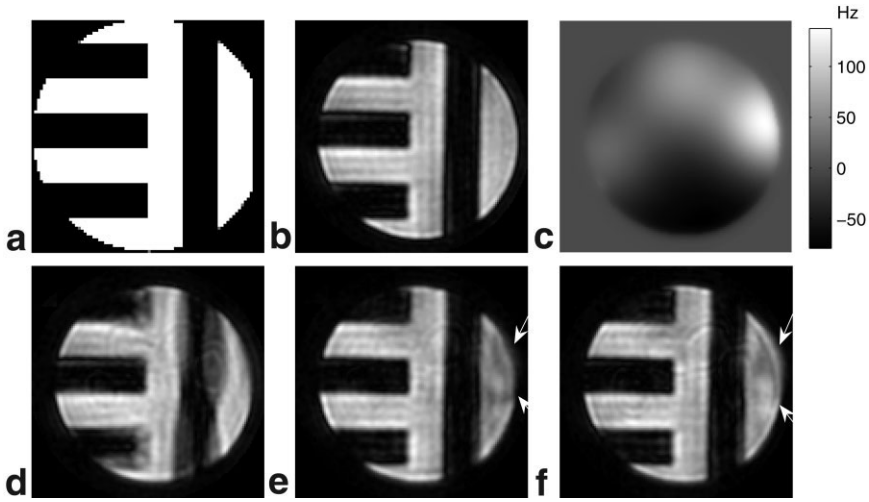


FIG. 12. **a:** Desired excitation pattern. **b:** Pattern obtained by an iteratively-designed pulse before metal pieces were attached to the phantom. **c:** Field map after attachment of the metal pieces. **d:** Pattern obtained by the pulse in **b**, distorted because of the inhomogenous field. **e:** Pattern obtained by the pulse designed with CP with field map incorporation. **f:** Pattern obtained by the iteratively designed pulse with field map incorporation. Field correction by the iterative method was slightly better in regions with a high off-resonance gradient (white arrows).

*k*-space, since aliasing was taken into account by the optimization scheme when it sought the cost-minimizing pulse. This important feature makes the iterative method stand out from noniterative ones. Second, iteratively designed pulses excited more accurately in spatial regions with large off-resonance gradients. This was partially attributable to the obviation of a DCF evaluation in the design process. As mentioned above, it is generally difficult to obtain an accurate DCF evaluation in the presence of large off-resonance gradients, and DCF errors contribute significantly to excitation error. The iterative method simply does not require the separate task of DCF evaluation.

We have also demonstrated the use of excitation error weighting for controlling excitation precision in different spatial regions. With the iterative method, designers can assign zero weights to "don't-care" regions and large weights to ROIs. In particular, assigning "don't-care" labels to uninteresting body regions, or regions with zero or low spin density (for example, outside-body regions) can boost precision in the ROIs.

In addition to improving precision, the iterative method can potentially lead to shorter pulse lengths, since undersampled *k*-space can be used with a lower penalty of excitation accuracy. In some applications (e.g., Ref. 2), slightly compromised overall excitation precision may be more tolerable than exceedingly lengthy pulses. Lastly, regularization can be used to trade excitation accuracy for a reduction in integrated and peak RF power. The global Tikhonov and local regularization techniques enable the designer to avoid suboptimal strategies (e.g., scaling or clipping) to make pulses implementable. RF power management could be crucial for high-field MRI.

The cost of all of these benefits is an increase in algorithm complexity and thus computational time. However, computational time was only a minor issue for our 2D designs. On our Linux system with a 3.2 GHz processor and 2 GB memory, the 15-iteration computation of the pulses in Fig. 5 took only 7.07 s. However, the computational time (and memory) required for pulse designs for volumetric selective excitation (e.g., Refs. 2 and 7) could be an issue. Algorithm acceleration can be achieved via time and frequency segmentation schemes (9,22,33), which make approximations to the off-resonance exponential factor in Eq. [3] so that the fast Fourier transformation (FFT) can be utilized. These acceleration techniques are currently under investigation.

There are several interesting possible extensions of the iterative design method. Joint optimization of the excitation *k*-space trajectory and RF pulse for a given desired pattern, inspired by the work of Hardy et al. (20), could potentially lead to a significant reduction in RF pulse length. Physical phenomena, such as spatial variations in RF coil sensitivity and RF field homogeneity, can be incorporated in the optimization formulation. This would readily benefit small-tip-angle selective excitation in multicoil transmit systems (5,6) and high-field imaging.

At a low cost in computational time, the iterative RF pulse design method offers advantages in terms of excitation precision, DCF obviation, potential pulse length reduction, and pulse power management. Our approach can benefit current applications of small-tip-angle selective excitation, and possibly foster future ones.

## ACKNOWLEDGMENTS

The authors thank Professor Matthew O'Donnell and Professor Romesh Saigal of University of Michigan for helpful discussions.

## APPENDIX

### Solution to the Inequality–Constrained Optimization Problem

The inequality-constrained optimization problem described by Eqs. [8] and [9] can be solved using the KKT theorem. The theorem states that if $\mathbf{b}^*$ is a regular point and a local minimizer to the problem, there exists nonnegative real Lagrange multipliers $\{\lambda_j^*\}_{j=0}^{N_t-1}$ such that for $j = 0, \ldots, N_t - 1$,

$$\lambda_j^* \cdot (|b_j^*|^2 - C) = 0, \qquad [11]$$

and the gradient of the Lagrangian function evaluated at $\mathbf{b}^*$ equals $\mathbf{0}$:

$$\nabla\{\|\mathbf{A}\mathbf{b}^* - \mathbf{d}\|_{\mathbf{W}}^2 + \beta\mathbf{b}^{*\prime}\mathbf{b}^* + \sum_{j=0}^{N_t-1} \lambda_j^*(|b_j^*|^2 - C)\} = \mathbf{0}. \quad [12]$$

Equations [11] and [12] must be solved simultaneously for the optimizer. One can use commercial optimization packages (for example, the Optimization Toolbox in Matlab) to tackle the problem, although conversion of the problem to a real-valued one may be necessary, and the process can be computationally expensive. If the multipliers are known a priori, $\mathbf{b}^*$ can be obtained, due to the convexity of the Lagrangian function, via

$$\mathbf{b}^* = \arg\min_{\mathbf{b}} \{\|\mathbf{A}\mathbf{b} - \mathbf{d}\|_{\mathbf{W}}^2 + \beta\mathbf{b}'\mathbf{b} + \mathbf{b}'\mathbf{\Lambda}^*\mathbf{b}\}, \quad [13]$$

where $\mathbf{\Lambda}^* = diag(\lambda_j^*)$.

## REFERENCES


1. Pauly JM, Nishimura DG, Macovski A. A *k*-space analysis of small-tip-angle excitation. J Magn Reson 1989;81:43–56.
2. Stenger VA, Boada FE, Noll DC. Three-dimensional tailored RF pulses for the reduction of susceptibility artifacts in $T_2$*-weighted functional MRI. Magn Reson Med 2000;44:525–531.
3. Rieseberg S, Frahm J, Finsterbusch J. Two-dimensional spatially-selective RF excitation pulses in echo-planar imaging. Magn Reson Med 2002;47:1186–1193.
4. Mohiaddin RH, Gatehouse D, Moon JC, Youssuffidin M, Yang GZ, Firmin DN, Pennell DJ. Assessment of reactive hyperaemia using real time zonal echo-planar flow imaging. J Cardiovasc Magn Reson 2002; 4:283–287.
5. Katscher U, Börnert P, Leussler C, van den Brink JS. Transmit SENSE. Magn Reson Med 2003;49:144–150.
6. Zhu Y. Parallel excitation with an array of transmit coils. Magn Reson Med 2004;51:775–784.
7. Saekho S, Boada FE, Noll DC, Stenger VA. Small tip angle three-dimensional tailored radiofrequency slab-select pulse for reduced B1 inhomogeneity at 3 T. Magn Reson Med 2005;53:479–484.
8. Pauly JM, Nishimura DG, Macovski A. A linear class of large-tip-angle selective excitation pulses. J Magn Reson 1989;82:571–587.
9. Noll DC, Meyer CH, Pauly JM, Nishimura DG, Macovski A. A homogeneity correction method for magnetic resonance imaging with time-varying gradients. IEEE Trans Med Imaging 1991;10:629–637.
10. Schomberg H. Off-resonance correction of MR images. IEEE Trans Med Imaging 1999;18:481–495.
11. Börnert P, Aldefeld B. On spatially selective RF excitation and its analogy with spiral MR image acquisition. Magn Reson Mater Phys Biol Med 1998;7:166–178.
12. Schomberg H, Börnert P. Off-resonance correction of nD spatially selective RF pulses. In: Proceedings of the 6th Annual Meeting of ISMRM, Sydney, Australia, 1998. p 2059.
13. Noll DC, Fessler JA, Sutton BP. Conjugate phase MRI reconstruction with spatially variant sample density correction. IEEE Trans Med Imaging 2005;24:325–336.
14. Pipe JG, Menon P. Sampling density compensation in MRI: rationale and an iterative numerical solution. Magn Reson Med 1999;41:179–186.
15. Conolly S, Nishimura DG, Macovski A. Optimal control solutions to the magnetic resonance selective excitation problem. IEEE Trans Med Imaging 1986;MI-5:106–115.
16. Murdoch JB, Lent AH, Kritzer MR. Computer-optimized narrowband pulses for multislice imaging. J Magn Reson 1987;74:226–263.
17. Conolly S. Magnetic resonance selective excitation. Ph.D. dissertation, Stanford University, Stanford, CA, 1989.
18. Lurie DJ. A systematic design procedure for selective pulses in NMR imaging. Magn Reson Imaging 1985;3:235–243.
19. O'Donnell M, Adams WJ. Selective time-reversal pulses for NMR imaging. Magn Reson Imaging 1985;3:377–382.
20. Hardy CJ, Bottomley PA, O'Donnell M, Roemer P. Optimization of two-dimensional spatially selective NMR pulses by simulated annealing. J Magn Reson 1988;77:233–250.
21. Harshbarger TB, Twieg DB. Iterative reconstruction of single-shot spiral MRI with off-resonance. IEEE Trans Med Imaging 1999;18:196–205.
22. Sutton BP, Noll DC, Fessler JA. Fast, iterative image reconstruction for MRI in the presence of field inhomogeneities. IEEE Trans Med Imaging 2003;22:178–188.
23. Munger P, Crelier GR, Peters TM, Pike GB. An inverse problem approach to the correction of distortion in EPI images. IEEE Trans Med Imaging 2000;19:681–689.
24. Bazaraa MS, Sherali HD, Shetty CM. Nonlinear programming. 2nd ed. New York: Wiley; 1993.
25. Glover GH. Simple analytic spiral *k*-space algorithm. Magn Reson Med 1999;42:412–415.
26. Spielman D, Pauly J, Macovski A, Enzmann D. Spectroscopic imaging with multidimensional pulses for excitation: SIMPLE. Magn Reson Med 1991;19:67–84.
27. Hoge RD, Kwan RK, Pike GB. Density compensation functions for spiral MRI. Magn Reson Med 1997;38:117–128.
28. Schneider E, Glover GH. Rapid in vivo proton shimming. Magn Reson Med 1991;18:335–347.
29. Schröder C, Börnert P, Aldefeld B. Spatial excitation using variable-density spiral trajectories. J Magn Reson Imaging 2003;18:136–141.
30. Stenger VA, Boada FE, Noll DC. Variable-density spiral 3D tailored RF pulses. Magn Reson Med 2003;50:1100–1106.
31. Nehrke K, Börnert P, Groen J, Smink J, Böck JC. On the performance and accuracy of 2D navigator pulses. J Magn Reson Imaging 1999;17: 1173–1181.
32. Fessler JA. Penalized weighted least-squares image reconstruction for positron emission tomography. IEEE Trans Med Imaging 1994;13:290–300.
33. Man LC, Pauly JM, Macovski A. Multifrequency interpolation for fast off-resonance correction. Magn Reson Med 1997;37:785–792.